Coulomb effect in laser-induced recollision excitation

T. Shaaran,* K. Z. Hatsagortsyan, and C. H. Keitel
Max-Planck-Institute für Kernphysik, Saupfercheckweg 1, D-69117 Heidelberg, Germany

(Received 16 January 2018; published 13 August 2018)

Our investigation considers the amended strong-field approximation (SFA) ionization of rare-gas atoms in a strong laser field accompanied by excitation of the atom due to laser-induced recollision. This process can be viewed as inelastic above-threshold ionization and corresponds to the recollision-excitation step of the laser-induced nonsequential double ionization via RESI (recollision excitation with subsequent ionization) mechanism. Within the SFA framework, up to now, Born approximation has been used to calculate the recollision-excitation process during RESI, which is not a good approximation at low-energy recollisions. In this work, we improve this model by employing Coulomb-Born approximation, where the recolliding electron is described with a Coulomb continuum wave function. We calculate the photoelectron momentum distributions (PMD) of the rescattered electron for helium and argon atoms by considering different excitation states. The Coulomb effect is shown to play a significant role for shaping the recollision-excitation probability, visible as in the fully differential PMD, as well as in the PMD integrated over transverse momenta.

DOI: 10.1103/PhysRevA.98.023410

I. INTRODUCTION

Electron correlations play an important role in the dynamics of atoms and molecules subjected to a strong laser field [1–4]. In particular, it has been employed for developing ultrafast molecular imaging [5–11]. Today, there is a general consensus that for linearly polarized laser field with infrared frequencies and high intensities, within 10^{13}–10^{15} W/cm^2, the strongly correlated electron motion in laser atom interaction is effectuated by laser-induced rescattering [12–14]. The rescattering is initiated by the tunneling of electron from atom. It gains energy during excursion in the laser field, is subsequently driven back by the laser field toward its parent ion, recollides with it, and as a result brings about the correlated dynamics of atomic electrons.

A particular consequence of the recollision in strong-field ionization dynamics is the initiation of nonsequential double ionization (NSDI), when the recolliding electron induces the ionization of the second electron of the atom [15,16]. The existence NSDI was demonstrated for the first time in the early 1980s, when the cross section of multiphoton ionization of xenon atoms was investigated [17,18], to measure the rate of ionization against the intensity of an external laser field. Subsequently this phenomenon has been observed for other noble gas atoms [19–28] and for molecules [29–31].

In the recollision process, the second electron may be dislodged by direct impact ionization, a $(e, 2e)$-like double ionization. Alternatively, it is first promoted to an excited bound state, which is ionized by the laser field afterwards. The latter mechanism consists of two steps: (1) recollision-induced excitation (RE) and (2) subsequent ionization (SI), together termed as recollision-induced excitation with subsequent ionization (RESI). The key features of RESI mechanism are pronounced at lower rescattering momenta. In this case the kinematically allowed region of the momentum components, parallel to the laser polarization axis of asymptotic photoelectrons, is located around $p_{1\parallel} = 2\sqrt{U_p}$ and $p_{2\parallel} = 0$, respectively, where U_p is the ponderomotive potential (average oscillatory energy) of the electron in the laser field. The $(e, 2e)$-like double ionization is a well studied mechanism and considerably easier to model in the context of semianalytical approaches [32–35], while RESI treatment is more elaborate. It is required to account for several effects, such as different excitation channels, multielectron effect of the bound state, depletion [36,37], quantum interference between all the available channels [38], and the possibility of creating a superposition of excited states at the time of rescattering. Moreover, the focal averaging and Coulomb focusing significantly modify photoelectron momentum distribution (PMD) for RESI. In addition, for multicycle laser pulses at near-infrared wavelength PMD of the correlated electrons in $(e, 2e)$ and RESI channels coexist and overlap with each other, which limits the detailed experimental investigation of the underlying processes.

There are several approaches for the RESI treatment. RESI has been calculated classically via classical trajectory Monte Carlo simulations [39–42], quasiclassically using S-matrix formalism based on strong-field approximation (SFA) [15,16], and by the so-called quantitative rescattering (QRS) method [36,37,43,44]. In the classical method it is not possible to include excitation in a rigorous way. This is accomplished by considering an *ad hoc* time lag between the rescattering of the first electron and ionization of the second electron. With this assumption both electrons leave with opposite momenta, yielding distributions mainly located in the second and fourth quadrants of PMD, rather than in all quadrants [40–42,45–50]. How the time delay may arise during excitation is not addressed in this treatment. As it was shown in [15], the electron-impact ionization with a time delay also can populate the low regions of electron momentum distributions. On the other hand, the RESI description based on SFA [51–55] and on QRS lead to electron momentum distributions in all

*Corresponding author: t.shaaran@yahoo.com

four quadrants, not just the second and the fourth quadrants [36,37].

In the QRS method, the RESI is calculated in three separate steps by employing a different theoretical method for each step [36,37]. For the first step SFA is used for calculation of the wave packet of the return electron. In the second step, the electron-impact excitation of ion is calculated by employing a laser-free differential cross section of the electron-impact excitation, with the electron's initial energy equal to that provided by the laser field at the time of rescattering. In the third step, the Perelomov-Popov-Terent'ev (PPT) ionization rate [56,57] is used to calculate tunneling ionization of the second electron. In this method, matching the return electron wave packet for all values of momentum components with its corresponding field free inelastic electron-impact excitation cross section as well as finding its corresponding shifts due to the laser field is very demanding. Up to now, the return electron wave packet with maximum return energy is mainly considered.

In contrast to the two previous methods, SFA provides a systematic description of RESI without additional heuristic assumptions, rigorously relating the initial bound state of the system to the final continuum state passing through intermediate excited states [58]. This comes from the fact that for a given NSDI process one can identify the most relevant Feynman diagrams that contribute to the transition amplitude and derive the relevant S matrix [59]. Furthermore, this method provides a transparent picture for NSDI mechanisms because the individual mechanism involved, such as electron-impact ionization and RESI, can be defined clearly from the outset. In addition, the classical trajectory of an electron in an external laser field can be directly connected with this method without loss of quantum-interference effects. These advantages make the SFA a powerful semianalytic method for describing NSDI, or strong-field phenomena in general. In fact, it gives good physical insight into the space-time picture of the system. However, the method has two main drawbacks: (1) the influence of the laser field is neglected when the electrons are bound to the atoms or molecules; (2) the binding ionic potential is neglected when the electrons are in the continuum. As a result, plane wave is used for treating the field-dressed inelastic electron-impact excitation cross section.

In this work we provide an improved description for the strong-field ionization accompanied by excitation of the atom due to laser-induced recollision, i.e., for inelastic above-threshold ionization (IATI). We employ amended SFA, where the recolliding electron in the field of the residual ion is described by a Coulomb continuum wave function in the SFA framework, rather than a plane wave that was the case in the common SFA. Although the RE is the first step of RESI, it has a separate physical interest connected with IATI, in which the laser-induced rescattering process creates an excited ion without subsequent ionization of the second electron. This process has not yet been experimentally identified because of the competing RESI channel. However, one may expect the RESI channel to be suppressed when using extremely short laser pulses. In this case the excited electron may not experience the field maximum, and the excited atomic state will survive up to the end of the laser pulse. It can be detected, for instance, by characteristic fluorescence. There is also the possibility to observe IATI at the tail of a long laser pulse, when the excited electrons experience relatively lower intensity and the ionization probability of the second electron is significantly low.

We calculate PMD of the laser-induced RE for different excitation channels and investigate the Coulomb field effect comparing our results with those of the common SFA (in the latter case a plane wave is used for the recolliding electron). We analyze the electron longitudinal momentum distribution at different fixed transverse momenta, as well as integrate over all transverse momenta. This provides good physical insight into the Coulomb effect for the individual quantum paths and its relation to the experimental measurements, since the integration over transverse momenta gives direct comparison with experimental outputs.

This work is organized as follows. In Sec. II A, we introduce the general expression for the SFA amplitude for laser-induced RE. The rescattering prefactor employing Coulomb-Born approximation is derived in Sec. II B. In Sec. III, the ion impact excitation cross section for Born and Coulomb-Born approximations are compared. Sections III A and III B present the PMD results of IATI for helium and argon atoms, respectively. Our conclusion is given in Sec. IV.

II. THEORY

A. Strong-field approximation: General formalism

The transition amplitude of laser-induced RE reads [52]

$$M(\mathbf{p}) = \int_{-\infty}^{\infty} dt'' \int_{-\infty}^{t''} dt' \int d^3k\, V_{\mathbf{p},\mathbf{k}} V_{\mathbf{k}} \times \exp[iS(\mathbf{p},\mathbf{k},t',t'')], \tag{1}$$

with the electron classical action

$$S(\mathbf{p},\mathbf{k},t',t'') = -\int_{t''}^{\infty} d\tau \frac{[\mathbf{p}+\mathbf{A}(\tau)]^2}{2} - \int_{t'}^{t''} d\tau \frac{[\mathbf{k}+\mathbf{A}(\tau)]^2}{2} + (E_2 - E_3)t'' + E_1 t', \tag{2}$$

where $\mathbf{A}(\tau)$ is the vector potential, E_1 is the ionization potential energy of the first electron, E_2 is the ground-state energy of the singly ionized atom, E_3 is the ionization potential energy of the state to which the second electron is excited, $\mathbf{p}$ is the final momenta of the electron, $\mathbf{k}$ is the intermediate momentum of the ionized electron, and $V_{\mathbf{k}}$ and $V_{\mathbf{p},\mathbf{k}}$ are the ionization and recollision matrix elements, respectively, given below.

The amplitude of Eq. (1) describes a physical process in which the first electron leaves the atom at a time t', propagates in the continuum with momentum $\mathbf{k}$ from t' to t'', and, upon returning, gives part of its kinetic energy to the core so that a second electron is promoted from a state with energy E_2 to an excited state with energy E_3. This electron then reaches the detector with a momentum $\mathbf{p}$.

The influence of the bounding potential and of the electron-electron interaction is embedded in the $V_{\mathbf{p},\mathbf{k}}$ and $V_{\mathbf{k}}$; they read

$$\begin{aligned} V_{\mathbf{p},\mathbf{k}} &= \langle \chi[\mathbf{p}+A(t'')], \varphi^{(n'l')} \left| \frac{1}{\mathbf{r}_{12}} \right| \chi[\mathbf{k}+A(t'')], \varphi^{(nl)} \rangle \\ &= \frac{1}{(2\pi)^3} \iint d^3\mathbf{r}_2 d^3\mathbf{r}_1 \chi[\mathbf{p}+A(t''),\mathbf{r}_1][\varphi^{(n'l')}(\mathbf{r}_2)]^* \\ &\quad \times \frac{1}{\mathbf{r}_{12}} \chi[\mathbf{k}+A(t''),\mathbf{r}_1]\varphi^{(nl)}(\mathbf{r}_2) \end{aligned} \tag{3}$$

and

$$V_{\mathbf{k}} = \langle \chi[\mathbf{k} + A(t')]|V|\varphi^{(gl)}\rangle = \frac{1}{(2\pi)^{3/2}} \int d^3\mathbf{r}\, e^{i[\mathbf{k}+A(t')\cdot\mathbf{r}]} V(r)\varphi^{(gl)}(\mathbf{r}), \quad (4)$$

where $\varphi^{(gl)}$ is the initial position-space wave function of the first electron in the ground state, $\varphi^{(nl)}$ and $\varphi^{(n'l')}$ are the wave functions of the second electron excited from the ground state (nl) of the target ion to the state $(n'l')$, respectively, and χ is the continuum wave function of the first rescattering electron.

For calculating the multiple integrals in Eq. (1), we employ saddle-point approximation. The saddle points of the integration variables t', t'', and $\mathbf{k}$, for which the action in Eq. (2) is stationary, are obtained from the saddle-point equations:

$$\begin{aligned} \partial S(\mathbf{p}, \mathbf{k}, t'', t')/\partial t' &= 0, \\ \partial S(\mathbf{p}, \mathbf{k}, t'', t')/\partial t'' &= 0, \\ \partial S(\mathbf{p}, \mathbf{k}, t'', t')/\partial \mathbf{k} &= 0, \end{aligned} \quad (5)$$

which yields

$$[\mathbf{k} + \mathbf{A}(t')]^2 = -2E_1, \quad (6)$$

$$\mathbf{k} = -\frac{1}{t'' - t'} \int_{t'}^{t''} \mathbf{A}(\tau) d\tau, \quad (7)$$

$$[\mathbf{p} + \mathbf{A}(t'')]^2 = [\mathbf{k} + \mathbf{A}(t'')]^2 - 2(E_2 - E_3). \quad (8)$$

The saddle-point Eq. (6) gives the conservation of energy at the instant t', corresponding to the tunneling ionization of the first electron; Eq. (7) constrains the intermediate momentum $\mathbf{k}$ of the first electron to enable its return to the parent ion; Eq. (8) expresses the energy conservation at the excitation of the second electron when the first electron returns to its parent ion at a time t'' and rescatters inelastically. One should note that the saddle-point Eq. (6) has a complex solution, with the imaginary part of the solution related to the ionization probability for the electron.

Once these solutions are obtained then one can determine the transition amplitudes

$$M(\mathbf{p}) = \sum_s \left(\frac{2\pi}{|\det S''(\mathbf{p}_s, \mathbf{k}_s, t'_s, t''_s)|} \right)^{5/2} V_{\mathbf{p},\mathbf{k}} V_{\mathbf{k}} \times \exp\{i S(\mathbf{p}_s, \mathbf{k}_s, t'_s, t''_s)\}, \quad (9)$$

where the index s runs over the relevant saddle points and $\det S''(\mathbf{p}_s, \mathbf{k}_s, t'_s, t''_s)$ gives the determinant of the 5×5 matrix of the second derivative of the action with respect to t', t'', and $\mathbf{k}$.

B. Coulomb effects

Within the SFA framework, up to now, Born approximation, i.e., plane wave, has been used for calculating the excitation prefactor $V_{\mathbf{p}e,\mathbf{k}g}$. For detailed discussion, see Ref. [51]. Although the plane wave could well explain the main feature of RESI, it fails at the threshold energy, where energy of the return electron is equal to the excitation energy of the target ion. For accurate treatment of the individual excitation channels one needs to go beyond this approximation. In this work, we overcome this shortage by employing the Coulomb-Born (CB) approximation [60,61]. In this approach the continuum state of the recolliding electron is described by the Coulomb wave function χ, which is the electron continuum eigenstate in the Coulomb field with an asymptotic momentum $\mathbf{K}$:

$$\chi(\mathbf{K}, \mathbf{r}) = e^{\frac{1}{2}\pi\alpha}\Gamma(1 - i\alpha)e^{-i\mathbf{K}\cdot\mathbf{r}} {}_1F_1\{i\alpha; 1; i(Kr + \mathbf{K}\cdot\mathbf{r})\}, \quad (10)$$

where $\alpha = 1/K$ and ${}_1F_1$ is the confluent hypergeometric function. For the states describing the electron before and after the rescattering $\mathbf{K} = \mathbf{k} + \mathbf{A}(t'')$ and $\mathbf{K} = \mathbf{p} + \mathbf{A}(t'')$, respectively.

For calculating Eq. (3), we use the expansion

$$\frac{1}{\mathbf{r}_{12}} = \sum_\lambda \rho_\lambda(\hat{\mathbf{r}}_1, \hat{\mathbf{r}}_2)\eta_\lambda(r_1, r_2), \quad (11)$$

with

$$\rho_\lambda(\hat{\mathbf{r}}_1, \hat{\mathbf{r}}_2) = \frac{4\pi}{2\lambda + 1} \sum_\mu Y^*_{\lambda\mu}(\hat{\mathbf{r}}_2) Y_{\lambda\mu}(\hat{\mathbf{r}}_1) \quad (12)$$

and

$$\eta_\lambda(r_1, r_2) = \begin{cases} \frac{r_1^\lambda}{r_2^{\lambda+1}} & \text{for } r_1 < r_2, \\ \frac{r_2^\lambda}{r_1^{\lambda+1}} & \text{for } r_1 > r_2, \end{cases} \quad (13)$$

where $Y_{\lambda\mu}$ are spherical harmonics and the vectors with hat are unit vectors along the corresponding vector. For the s-p transition only the dipole term $\lambda = 1$ contributes, while for the p-d transition both $\lambda = 1$ and 3 contribute but the dipole term gives the dominant contribution. For the p-p transition both $\lambda = 0$ and 2 contribute but the term with $\lambda = 0$ gives the dominant contribution.

Furthermore, for the Coulomb wave function we also use a partial wave expansion

$$\chi(\mathbf{K}, \mathbf{r}) = K^{1/2} r^{-1} \sum_L i^L (2L + 1) e^{i\sigma_L} \chi_L(K, r) P_L(\hat{\mathbf{r}}, \hat{\mathbf{K}}), \quad (14)$$

with

$$P_L(\hat{\mathbf{r}}, \hat{\mathbf{K}}) = \sum_M \frac{4\pi}{2L + 1} Y^*_{LM}(\hat{\mathbf{K}}) Y_{LM}(\hat{\mathbf{r}}) \quad (15)$$

and

$$\chi_L(K, r) = \frac{\Gamma(L + 1 - i/K)}{2\sqrt{K}(2L + 1)!} e^{\pi/2K} (2Kr)^{L+1} e^{iKr} \times {}_1F_1(L + 1 - i/K; 2L + 2; -2iKr), \quad (16)$$

where $\sigma_L = \arg[\Gamma(L + 1 - i\alpha)]$ and P_L is the Legendre polynomial. Using the expansions of Eqs. (11) and (14), we decompose the matrix element Eq. (3) into the angular and the radial integrals:

$$V_{\mathbf{p},\mathbf{k}} = \sum_\lambda \sum_{L,L'} \mathrm{Re}_\lambda f_\lambda, \quad (17)$$

with

$$\mathrm{Re}_\lambda = \int_0^\infty \chi_L[p_1 + A(t''), r_1]\chi_{L'}[k + A(t''), r_1] \times \int_0^\infty \eta_\lambda(r_1, r_2)\varphi^{(n'l')}(r_2)\varphi^{(nl)}(r_2) dr_2 dr_1. \quad (18)$$

By following the theory of the spherical harmonics and the Racah coefficients we will have

$$f_\lambda = (-1)^{l+l'-L^T}[(2L+1)(2L'+1)(2l+1)(2l'+1)]^{1/2} \times (2\lambda-1)^{-1} C_{000}^{LL'\lambda} C_{000}^{ll'\lambda} W[LlL'l';L^T\lambda], \quad (19)$$

where $C_{000}^{LL'\lambda}$ and $C_{000}^{ll'\lambda}$ are Clebsch-Gorden coefficients and $W[LlL'l';L^T\lambda]$ is the Racah coefficient with $L^T = L + l$. The coefficients of f_λ can be obtained from the tables provided by Percival and Seaton in Ref, [39].

In the radial integral of Eq. (18), we use hydrogenlike wave functions, with an effective charge $z^* = \sqrt{2n^2 E_n}$, to describe the radial wave function of the bound state $\varphi^{(nl)}(r_n)$. Defining

$$\eta_\lambda(r_1) = \int_0^\infty \eta_\lambda(r_1, r_2)\varphi^{(n'l')}(r_2)\varphi^{(nl)}(r_2)dr_2, \quad (20)$$

and using the expansion of Eq. (13), we have

$$\eta_\lambda(r_1) = \frac{1}{r_1^{\lambda+1}}\int_0^{r_1} \varphi^{(n'l')}(r_2)\varphi^{(nl)}(r_2)r_2^\lambda dr_2 + r_1^\lambda \int_{r_1}^\infty \varphi^{(n'l')}(r_2)\varphi^{(nl)}(r_2)\frac{1}{r_2^{\lambda+1}}dr_2. \quad (21)$$

Furthermore, we can decompose the integral in Eq. (21) into two terms, with steeply and slowly decreasing integrands:

$$\eta_\lambda(r_1) = \frac{1}{r_1^{\lambda+1}}\int_0^\infty \varphi^{(n'l')}(r_2)\varphi^{(nl)}(r_2)r_2^\lambda dr_2 + \xi_\lambda(r_1), \quad (22)$$

with

$$\xi_\lambda(r_1) = r_1^\lambda \int_{r_1}^\infty \varphi^{(n'l')}(r_2)\varphi^{(nl)}(r_2)r_2^\lambda \frac{1}{r_2^{\lambda+1}}dr_2 - \frac{1}{r_1^{\lambda+1}}\int_{r_1}^\infty \varphi^{(n'l')}(r_2)\varphi^{(nl)}(r_2)r_2^\lambda dr_2. \quad (23)$$

The latter allows us to express the radial integral Re_λ as a sum of two integrals:

$$\mathrm{Re}_\lambda = \int_0^\infty \varphi^{(n'l')}(r_2)\varphi^{(nl)}(r_2)r_2^\lambda dr_2 \times \left\{\int_0^\infty \chi_L[p_1 + A(t''), r_1]\chi_{L'}[k + A(t''), r_1]\frac{1}{r_1^{\lambda+1}}dr_1 + \int_0^\infty \chi_L[p_1 + A(t''), r_1]\chi_{L'}[k + A(t''), r_1]\xi_\lambda(r_1)dr_1\right\}. \quad (24)$$

The first term of Eq. (24) can be evaluated analytically. The second term is calculated numerically as it converges rapidly. For more details we refer to Refs. [60,61].

III. RESULTS

In this section, we will compute the electron-impact excitation cross section and the probability for laser-induced RE based on CB approximation, which will be compared with the SFA results with the Born approximation. We approximate the external laser field by a monochromatic wave:

$$\mathbf{E}(t) = \hat{\mathbf{e}}_x E_0 \sin\omega t. \quad (25)$$

We also consider the tunneling prefactor $V_\mathbf{k}$ to be constant, since it does not change the shape of the electron momentum distributions and it is the same for all the considered excitation channels of given species. The electron-impact excitation cross section is

$$\sigma = \int \frac{|\mathbf{p} + A(t)|}{|\mathbf{k} + A(t)|}|V_{\mathbf{p},\mathbf{k}}|^2 d\Omega, \quad (26)$$

with the integration over the electron-scattering solid angle Ω.

The PMD of the laser-induced RE is given by $F(p_\parallel, p_\perp) = |M(\mathbf{p})|^2$. We calculate also PMD integrated over the transverse momentum components

$$F(p_\parallel) = \int |M(\mathbf{p})|^2 dp_\perp. \quad (27)$$

We consider helium and argon atoms because the first is easier to calculate theoretically and the other one is easier to measure experimentally. In here, we assume the helium atom is exposed to the monochromatic laser field with wavelength of 800 nm (0.057 a.u.) and intensity of $I = 3.5\times10^{14}$ W/cm^2 and argon atoms are exposed to the same monochromatic laser field but with the intensity of $I = 1.5\times10^{14}$ W/cm^2. These are typical intensities for the existed RESI experiments.

A. Helium

In this section we consider RE with helium atom. When helium atom is exposed to the laser field, the electron which is bound in $1s$ state with an ionization potential of $E_1 = 0.91$ a.u. tunnels through the barrier. After accelerating in the field it returns to the core and excites the second electron, which is bound to the core at $1s$ state with an ionization potential of $E_2 = 2.0$ a.u., to the either $2s$ or $2p$ states at $E_3 = 0.5$ a.u.

The electron recollision energy depends on the recollision time. The latter determines also the asymptotic longitudinal momentum (momentum component parallel to the laser polarization axis) of the photoelectron. To have an idea on the allowed region of recollision energies and asymptotic photoelectron longitudinal momenta, we show in panel (a) of Fig. 1 the rescattering times for the electron as functions of its longitudinal momentum $p_{||}$. The vertical axis shows the real rescattering time of the first electron in comparison to its tunnel

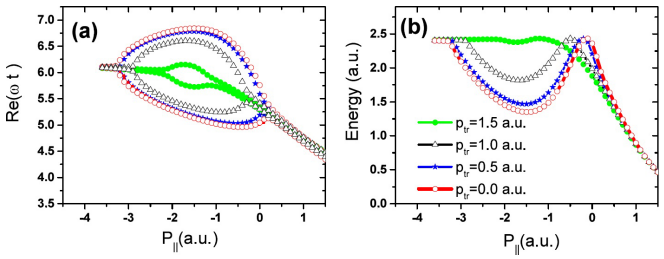

FIG. 1. Electron rescattering parameters vs electron asymptotic longitudinal momenta $p_{||}$ for the different fixed transverse momentum $p_\perp$ [indicated in (b)]: (a) real rescattering time; (b) recollision energy. The helium atom is exposed to the laser field with wavelength of 800 nm and intensity of $I = 3.5\times10^{14}$ W/cm^2. The excitation channels are $1s \to 2s$ and $1s \to 2p$. Connected scattered points and nonconnected scattered points in (a) correspond to the short and long trajectories, respectively.

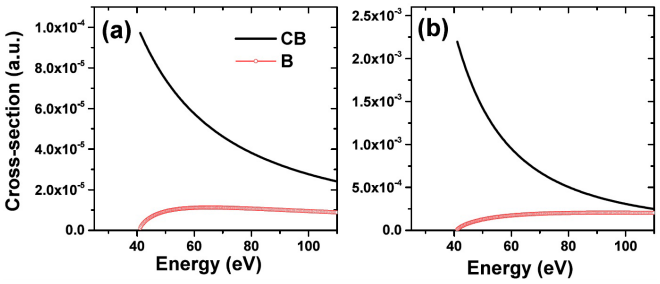

FIG. 2. Electron-impact excitation cross section of helium ion as a function of the incident energy of the rescattered electron: (a) $1s \rightarrow 2s$ excitation; (b) $1s \rightarrow 2p$ excitation. "B" and "CB" indicate Born and Coulomb-Born approximations, respectively.

ionization, which occurs at about a cycle earlier. In here, the panel (b) depicts the energy of the electron on its return to the core as a function of $p_{||}$. Both panels demonstrate the boundary of the classically allowed region for different fixed transverse momentum components. For rescattering time these boundaries are defined when the long (nonconnected scattered points) and the short trajectories (connected scattered points) merge together in panel (a). Then, we can find the boundary region of longitudinal momenta for each given transverse momentum. For instance, for the transverse momentum of $p_\perp = 0$, the classical allowed region for the longitudinal momentum is $p_{||} \approx (-3, 0.25)$ a.u. For the momentum beyond these two boundary points there is no classical counterpart. As a result the transition amplitude decays dramatically. Accordingly, one can also find the allowed region of the rescattering energy from panel (b). The maximum rescattering energy here is about 2.43 a.u. As we move towards larger transverse momenta, the classical allowed region of energy decreases until it completely disappears. In here at about $p_\perp = 1.5$ a.u. the classically allowed region of energy vanishes.

To understand how efficient RE can be in the kinematically allowed region, we calculate the cross section of the electron-impact excitations for $1s \rightarrow 2s$ and $1s \rightarrow 2p$ transitions as a function of incident energy according to Eq. (26) and show it in Fig. 2. For both excitation channels, around threshold energy $\triangle E = E_2 - E_1 \sim 40$ eV, the Born approximation (red connected scattered points) underestimates the cross section. It gives the maximum value for the cross section at about 50 eV and it decreases as we move towards the threshold energy. On the other hand, with Coulomb-Born approximation (black line) the cross-section value increases when moving towards threshold energy, which is the typical behavior for the cross section in the Coulomb field.

We also calculate the amplitude of the excitation prefactor $|V_{\mathbf{p}e,\mathbf{k}g}|^2$ given by Eq. (3) as a function of rescattered longitudinal momentum for different fixed transverse momentum components; see Fig. 1. For Born approximation at $p_\perp = 0$, the maxima (indicated by arrows) are around $p_{||} = -0.1$ a.u. for both $1s$ to $2s$ and $1s$ to $2p$ as shown in panels (a) and (c) in Fig. 3. These are very close to the cutoff momenta, which corresponds to the boundary of the classically allowed region as demonstrated in Fig. 1. In contrast to that the CB approximation predicts the maxima to be at about $p_{||} = -1.5$ a.u. in the $p_\perp = 0$ case for both $1s$ to $2s$ and $1s$ to

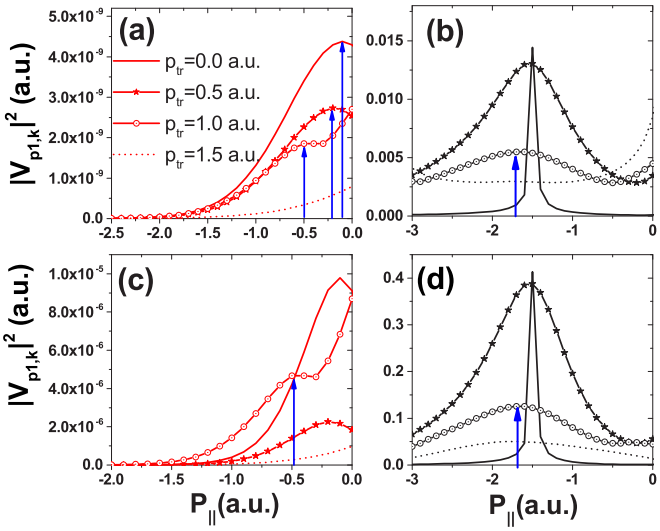

FIG. 3. Amplitude of the excitation prefactor $|V_{\mathbf{p}e,\mathbf{k}g}|^2$ via Eq. (3) for helium atom vs longitudinal momentum at fixed transverse momentum. The upper panels correspond to the excitation from $1s$ to $2s$, while the lower panels give the excitation from $1s$ to $2p$. The red and black lines (left and right columns) represent calculations based on Born and Coulomb-Born approximations, respectively. For visibility, the amplitude for $p_\perp = 0.5$, $p_\perp = 1$, and 1.5 a.u. in panels (b) and (d) are multiplied by 35 and 50, respectively. The amplitude for $p_\perp = 1$ and 1.5 a.u. in panels (a) and (c) are multiplied by 3 and 50, respectively. The laser parameters are the same as in Fig. 1.

$2p$ transitions, as demonstrated in panels (b) and (d) in Fig. 3, i.e., compared to the Born approximation, the maxima shifted by 1.4 a.u. towards the middle of the classically allowed region. As we move towards larger transverse momenta the maxima slowly shift towards larger negative longitudinal momenta in both Born and CB approximations. For instance, at $p_\perp = 0.5$, the maxima in Born approximation are at a bound $p_{||} = -0.5$ a.u. The yield decrease as functions of $p_\perp$ with gradual drop up to $p_\perp = 1$ a.u. and follow with very sharp drop. The sharp drop exists in CB approximation, however, at much lower transverse momenta ($p_\perp = 0.5$ a.u.). While in the Born approximation at $p_\perp > 1.0$ a.u. the drop for excitation from $1s$ to $2p$ is much larger, the CB shows not very different drop for both $1s$ to $2p$ and $1s$ to $2s$ channels.

By employing Eq. (1), we calculate the RE probability $|M(\mathbf{p})|^2$ as a function of rescattered momentum components parallel to the laser polarization for the different fixed transverse momentum components. These calculations are demonstrated in Fig. 4. To fully investigate the contributions of the rescattering prefactor, we compute the transition amplitude with constant rescattering prefactor ($V_{\mathbf{p}e,\mathbf{k}g} = \text{const}$) for excitations from $1s$ to $2s$ [panel (a)] and to $2p$ [panel (b)]. For given transverse momentum, the two maxima correspond to the cutoff representing the boundaries of the classically allowed region as discussed in Fig. 1. The yield steadily increases as a function of the $p_\perp$. The transition amplitude has a minimum within the classically allowed region. In general, by including the prefactor these minima disappear. The prefactor derived from Born approximation strongly damps the maxima at lower momenta and preserves the second maxima almost at the same position as shown in panels (b) and (e). In addition, the

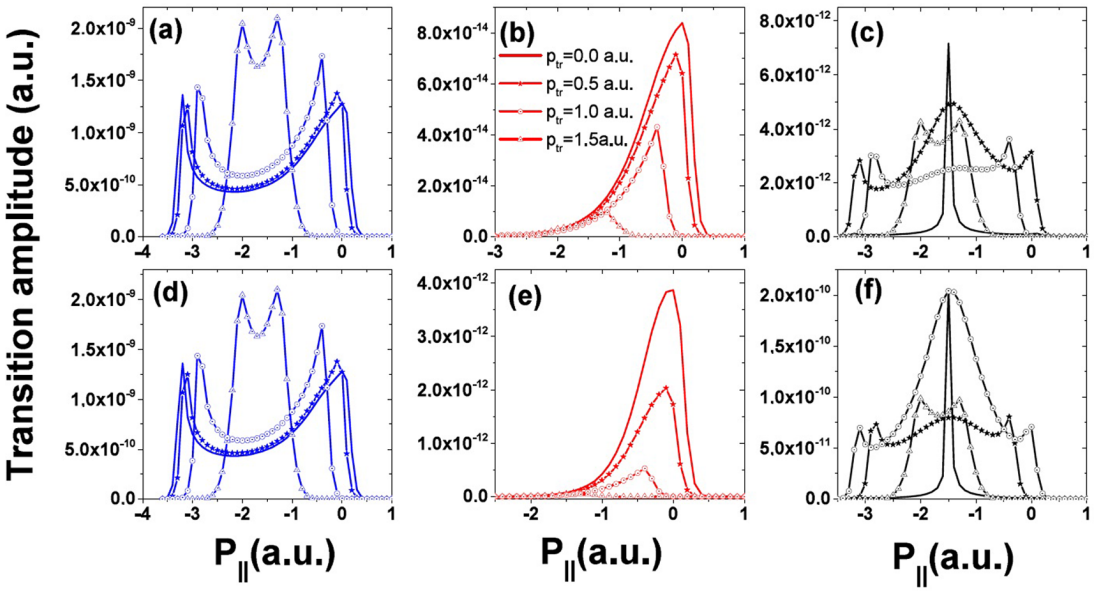

FIG. 4. RE probability $|M(\mathbf{p}_1)|^2$ for helium via Eq. (1) vs electron longitudinal momentum for fixed transverse momentum. The upper panels correspond to the excitation from $1s$ to $2s$, while the lower panels to the excitation from $1s$ to $2p$. The red and black lines (middle and right columns) represent calculations based on Born approximation and CB approximation, respectively, while blue line (left column) gives the transition amplitude with constant rescattering prefactor ($V_{\mathbf{p}_1 e,\mathbf{k}g} = \text{const}$). For visibility, the amplitudes of the rescattering prefactor for $p_\perp = 0.5$, 1, and 1.5 a.u. are multiplied by 25 for excitation to $2s$ [panel (c)] and 50 for excitation to $2p$ [panel (f)]. The laser parameters are the same as in Fig. 1.

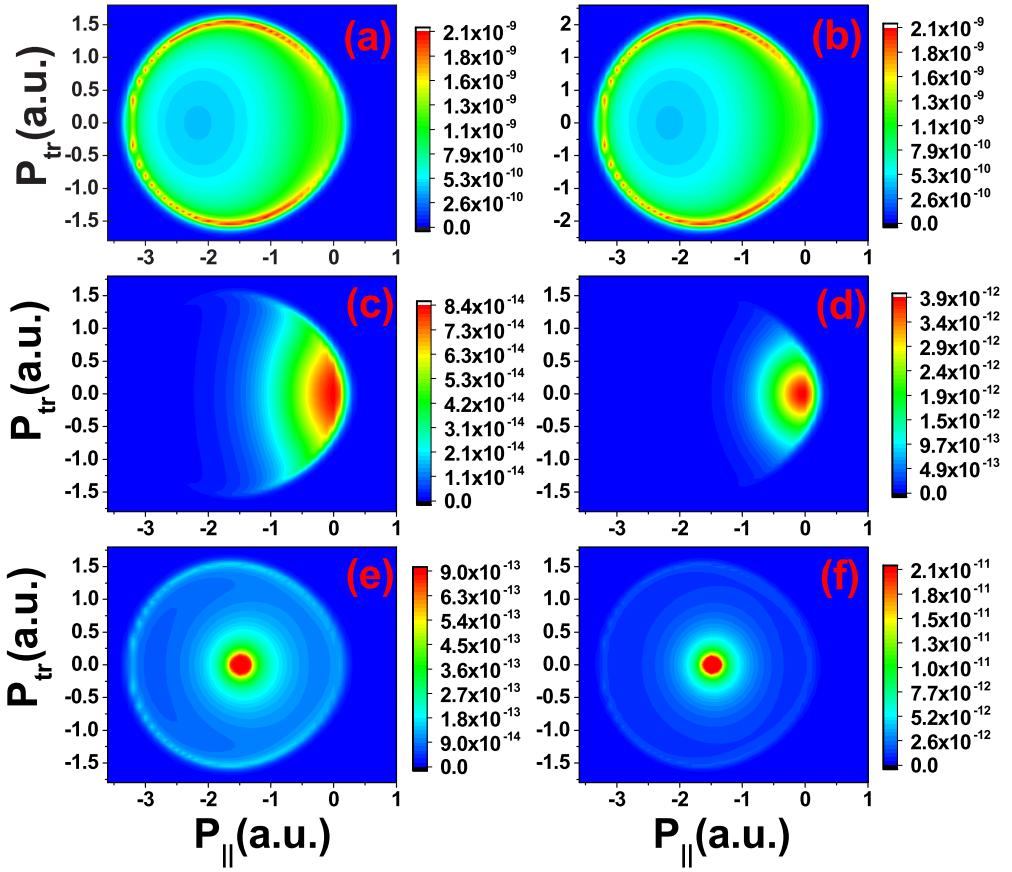

FIG. 5. PMD of RE for helium: left column gives the excitation from $1s$ to $2s$ state; right column gives the excitation from $1s$ to $2p$ state. The top panels show PMD with constant excitation prefactor ($V_{\mathbf{p}e,\mathbf{k}g} = \text{const}$), the middle panels with Born approximation, and the bottom panels with CB approximation. The laser parameters are the same as in Fig. 1.

prefactor affects the yield of the transition amplitude in that it decreases as a function of the transverse momenta. This can be understood if we look at the amplitude of the excitation prefactor calculated in the previous Fig. 3.

On the other hand, the prefactor derived from CB approximation reshapes the transition amplitude by shifting the position of the maxima towards the center of the classically allowed region ($p_\parallel = -1.5$) a.u. It happens because at this longitudinal momentum the energy of the return electron is close to the excitation threshold. As we demonstrate in Fig. 2 for Born approximation cross section is large at higher incident energy which relates to the momenta being closer to zero as shown in panel (b) of Fig. 1. Like Born approximation the yield of the transition amplitude decreases as a function of $p_\perp$ and it drops faster at larger transverse momenta. Moreover, for $p_\perp = 0$, which is the dominant channel, the overall yield for CB approximation is two orders of magnitude larger than Born approximation.

The full PMD for RE in the case of helium is shown in Fig. 5. The panels in the first column correspond to the excitation from $1s$ to $2s$, while the panels in the second column give the excitation from $1s$ to $2p$. For the photoelectron momentum distributions with constant excitation prefactor ($V_{\mathbf{p}e,\mathbf{k}g} = \text{const}$) (top panels) the main signal creates a ring with the strong signals located at its circumference at about $p_\parallel = -1$ a.u. and $p_\perp = \pm 1.5$ a.u. For the Born approximation (middle panels), these signals are mainly concentrated at the center where $p_\parallel = p_\perp \sim 0$ a.u. Meanwhile, for CB approximation (bottom panels) the maximum signals are at about $p_\parallel = -1.5$ a.u. and $p_\perp = 0$. From the results in Figs. 4 and 5, we can see that the main signals come from the $p_\perp = 0$ case.

We also calculate the RE probability integrated over transverse momenta via Eq. (27); see Fig. 6. The integration over transverse momenta is very useful from an experimental point of view and it provides better insight to what experimentally is measured in RESI. For the case with constant excitation prefactor, the integration over the transverse momenta wash out the minima observed for fixed transverse momenta shown in panels (a) and (d) of Fig. 4. It leads to the formation of the maximum at larger longitudinal momenta. Indeed for both $1s$ to $2s$ [panel (a)] and $1s$ to $2p$ [panel (d)] the peaks are

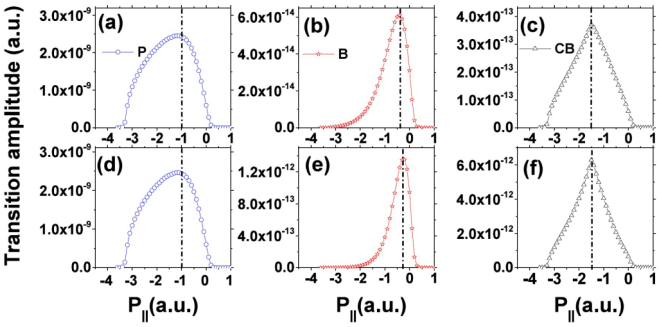

FIG. 6. RE probability for helium atom integrated over transverse momenta: upper panels correspond to the $1s$ to $2s$ excitation and lower panels to the $1s$ to $2p$ excitation. The red and black lines (middle and right columns) represent calculations based on Born approximation and CB approximation, respectively, and the blue line (left column) the calculation with constant excitation prefactor ($V_{\mathbf{p}e,\mathbf{k}g} = \text{const}$).

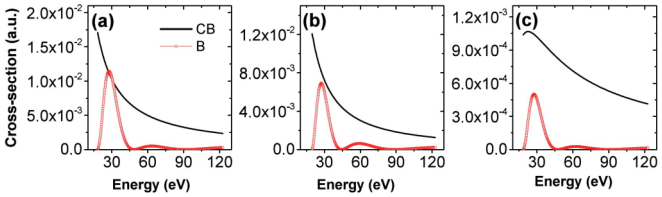

FIG. 7. Electron-impact excitation cross section of argon ion as a function of the incident energy of the rescattered electron: (a) excitation of $3p$ to $4s$, (b) excitation of $3p$ to $4p$, and (c) excitation of $3p$ to $3d$. For visibility in panels (a) and (b) the Born approximation cross-section results are multiplied by 20.

located at about $p_\parallel = -1.0$ a.u. For the Born approximation for both $1s$ to $2s$ [panel (b)] and $1s$ to $2p$ [panel (e)] the peaks at low momenta, $p_\parallel = 0$, survive. This corresponds to $p_\perp = 0$, as shown in panels (b) and (e) of Fig. 4. For CB approximation the peaks are formed at $p_\parallel = -1.5$ a.u. for both $1s$ to $2s$ [panel (c)] and $1s$ to $2p$ [panel (f)]. These are related to the peaks observed for the fixed transverse momentum of $p_\perp = 0$ as demonstrated in panels (c) and (f) in Fig. 4. Our calculations show that there is about 1.5 a.u. difference between the location of the peaks for Born and CB approximation. On the other hand, comparing CB transition amplitude with constant prefactor calculations (simple man model) shows a difference of only 0.5 a.u. It means the Born approximation is not appropriate for calculating RE and it leads to larger discrepancy than the simple man model.

B. Argon

Now we discuss the case of RE in argon. In argon the first electron on its return to the core excites the second electron

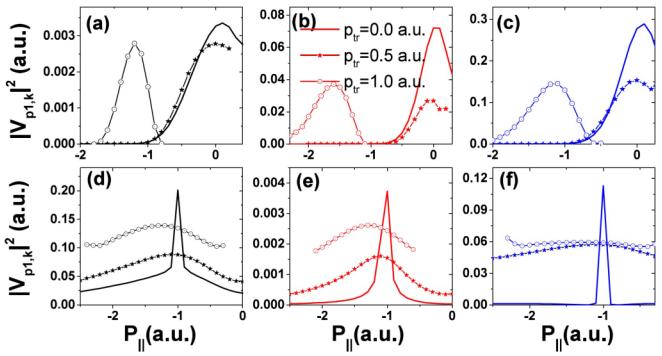

FIG. 8. Amplitude of the excitation prefactor $|V_{\mathbf{p}e,\mathbf{k}g}|^2$ via Eq. (3) as a function of electron longitudinal momentum for fixed transverse momentum components: first column, excitation of $3p$ to $4s$; second column, excitation of $3p$ to $4p$; third column, excitation of $3p$ to $3d$. The red and black lines (middle and left column) represent calculations based on Born approximation and CB approximation, respectively, while blue lines (right column) show the calculations with constant excitation prefactor ($V_{\mathbf{p}e,\mathbf{k}g} = \text{const}$). The argon atom is exposed to the monochromatic laser field with wavelength of 800 nm and intensity of $I = 1.5\times10^{14}$ W/cm^2. For visibility, in panel (a) the amplitudes of the excitation prefactor for $p_\perp = 0.5$ and 1 a.u. are multiplied by 5 and 5000, respectively. In panels (b) and (c) $p_\perp = 0.5$ and 1.0 a.u. are multiplied by 10 and 10 000, respectively. In panel (d) the amplitudes of the excitation prefactor for $p_\perp = 0.5$ and 1.0 a.u. are multiplied by 2 and 5, respectively, while in panels (e) and (f) they are respectively multiplied by 10 and 50.

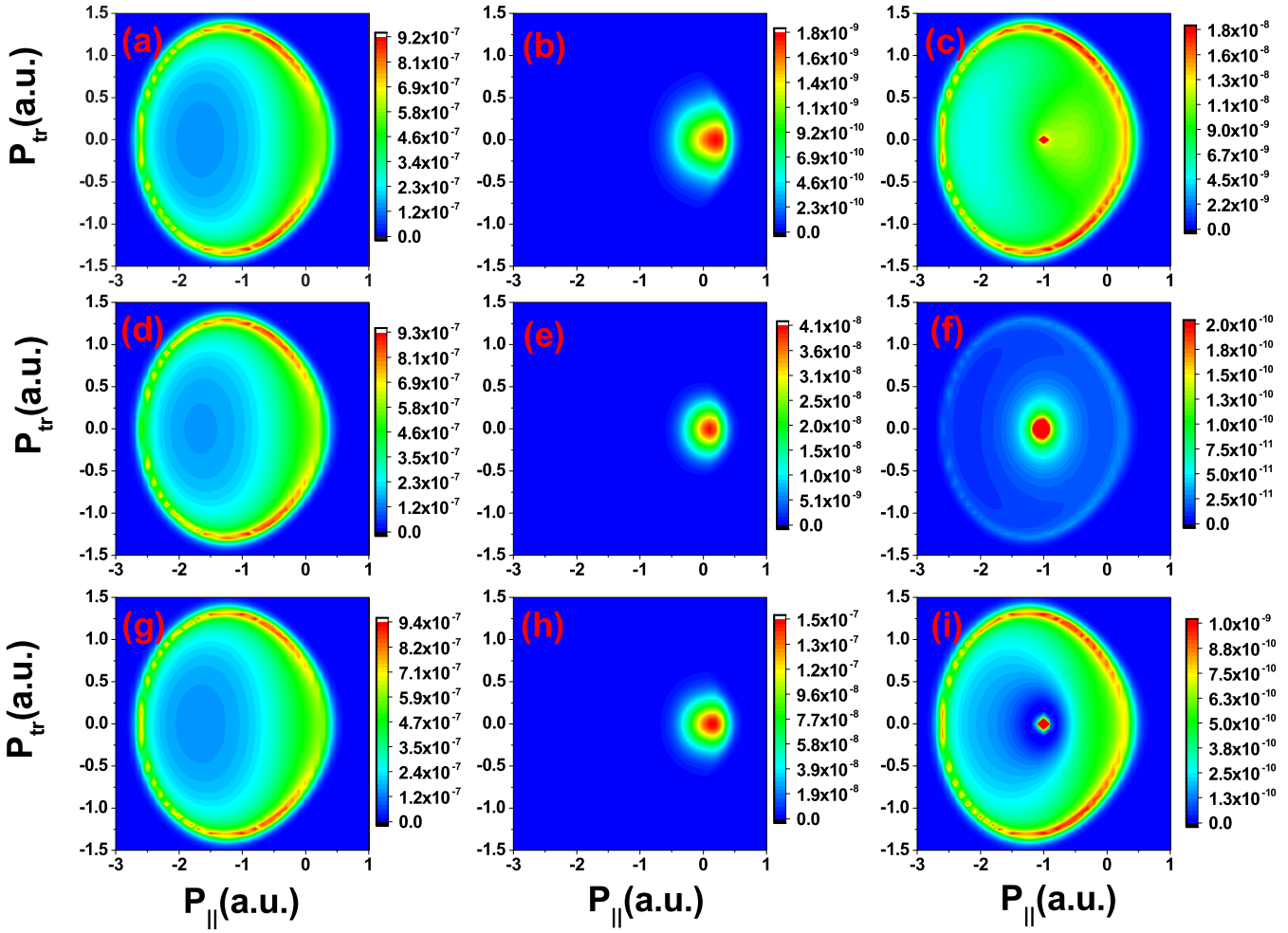

FIG. 9. PMD of RE for argon atom for the same parameters as in the previous figures. The panels in the top, middle, and bottom rows correspond to the excitation from $3p$ to $4s$, $4p$, and $3d$, respectively. The first column gives PMD with constant excitation prefactor ($V_{\mathbf{p}e,\mathbf{k}g} = \text{const}$), while the second and third columns are based on Born and CB approximation, respectively. The laser parameters are the same as in Fig. 8.

from $3p$ state with energy $E_1 = 1.02$ a.u. to the excited state $4s$ with $E_1 = 0.35$ a.u., or to the $4p$ state with $E_1 = 0.30$ a.u., or to the $3d$ state with $E_1 = 0.34$ a.u.

We show the excitation cross sections in Fig. 7. For all excitation channels, around threshold energy, $\triangle E = E_2 - E_1$, the Born approximation (red connected scattered points) underestimate the cross section. They give the maximum value for the cross section at larger incident energy than the threshold energy. In comparison to helium (Fig. 2) the results are more deviating from CB approximation at the threshold energy. In addition, the atomic structure of argon leads to another small peak at a bit larger incident energy. In this approximation describing the bound state of the argon by the hydrogenlike wave function leads to creation of these artificial peaks. On the other hand, with CB approximation (black line) the cross section decreases monotonously with increasing energy from the threshold value. Thus for argon atom Born approximation is not an appropriate one and one needs to consider the Coulomb effect.

The amplitude of the excitation prefactor $|V_{\mathbf{p}_1 e,\mathbf{k}g}|^2$ for argon atom as a function of the electron longitudinal momentum for different fixed transverse momentum components is shown in Fig. 8. Let us indicate the difference of the Born approximation results with respect to CB approximation. Overall, for Born approximation at $p_\perp = 0$ the maxima are at about $p_\parallel = 0.2$ a.u. As we move towards larger transverse momenta the maxima slowly shift towards larger negative longitudinal momenta. For $p_\perp = 0.5$, these maxima for $3p$ to $4s$ and $3p$ to $3d$ are at around $p_\parallel = -1.2$ a.u., while for $3p$ to $4p$ this is at about $p_\parallel = -1.5$ a.u. Like the helium case, the yield decreases as a function of $p_\perp$ but the sharp drop starts at very small transverse momentum ($p_\perp = 0.5$ a.u.). The fall of the transition amplitude yields for $3p$ to $4p$ and $3p$ to $3d$ is larger than that for $3p$ to $4s$. In distinction to that, in CB approximation for all cases at $p_\perp = 0$, the maxima are at about $p_\parallel = -1$ a.u. as shown in panels (d), (e), and (f). Like with Born approximation as we move towards larger transverse momenta the maxima slowly shift towards larger negative longitudinal momenta. The yield decreases as a function of $p_\perp$ with a sharp drop at low transverse momenta.

PMD for RE in the case of argon is represented in Fig. 9. The panels in the top, middle, and bottom rows correspond to the excitation from $3p$ to $4s$, $4p$, and $3d$, respectively. For the photoelectron momentum distribution with constant rescattering prefactor ($V_{\mathbf{p}e,\mathbf{k}g} = \text{const}$) (first column) the main signals create a ring with the largest signals located at its circumference at about $p_\parallel = 1.2$ a.u. and $p_\perp = \pm 1.3$ a.u. For the Born approximation (middle column), these signals are

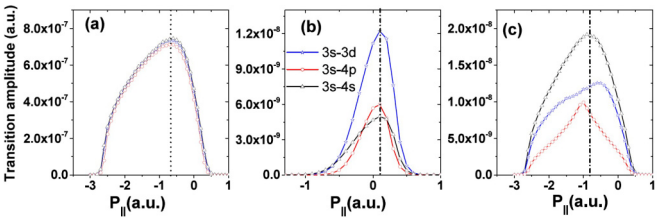

FIG. 10. RE probability for argon atom integrated over photoelectron transverse momenta: (a) PMD with constant prefactor ($V_{\mathbf{p}_1 e,\mathbf{k}g} = \text{const}$), (b) Born approximation, and (c) CB approximation. Black line shows the transition from $3p$ to $4s$, blue the transition from $3p$ to $3d$, and red lines the transitions from $3p$ to $4p$. The laser parameters are the same as in Fig. 8.

mainly concentrated at the center with $p_\parallel = p_\perp \sim 0$. For the CB approximation (third column) for all excitation channels there are strong signals at about $p_\parallel = -1$ a.u. and $p_\perp = 0$, surrounded by a ring. For $3p$ to $4s$ and $3d$ there are robust signals along the circumference of the ring, but for $3p$ to $4p$ these signals are very weak.

The PMD integrated over transverse momenta are depicted in Fig. 10. For the case with constant prefactor the peaks for all three excited states are at about $p_\parallel = -0.6$ a.u. [panel (a)]. For Born and CB approximation these peaks are around $p_\parallel = 0.2$ a.u. and $p_\parallel = -1$ a.u., respectively. There is 1.25 a.u. shift between results of Born and CB approximations, while the difference between constant prefactor and CB is smaller, about 0.5 a.u. This means the simple man model gives a better result than Born approximation. For the constant prefactor, the yield for all three excitation channels is the same. This comes from the fact that the excitation energies of these cases are very close and they take place at the same laser phase from the simple man model point of view. For Born approximation, $3p$ to $3d$ has larger yield and the two other excitation channels have lower yield. Meanwhile, in the CB approximation the $3p$ to $4s$ transition is associated with a larger yield followed by $3p$ to $3d$, and $3p$ to $4p$.

IV. CONCLUSIONS

We have investigated the role of the Coulomb field of the residual ion for the photoelectron momentum distribution in the process of an ionization of helium and argon atoms in a strong laser field accompanied by excitation of the atomic ion due to laser-induced recollision. The calculations are carried out in the framework of SFA with an amended recollision amplitude. The effect of the Coulomb field is accounted for by replacing the incoming plane wave for the recolliding electron, as it was the case in the common SFA, with the Coulomb continuum wave function in computing of the electron-impact excitation amplitude.

We estimate the excitation cross section for helium and argon atoms and show that the Born approximation fails at the threshold energies. The failure in the case of an argon atom is more noticeable. The derived recollision-excitation probability using the Coulomb-Born approximation provides physically relevant behavior with respect to the recollision energy. The latter changes significantly the asymptotic photoelectron momentum distribution with respect to the common SFA result. The Coulomb field effect reshapes photoelectron momentum distribution and shifts the position of the maxima towards the center of the classically allowed region, while in the Born approximation the PMD peaks are mainly formed at the cutoff of the classically allowed region which is closer to zero.

We employed also a simple man model for the process, approximating the excitation amplitude with a constant factor. What is surprising is that the rough simple man model provides photoelectron momentum distribution closer to the result of the accurate Coulomb-Born approximation than the common SFA with Born approximation for the recollision amplitude. In the simple man model the photoelectron momentum distributions of the recollision-excitation process form a ring where the signals are mainly located at its circumference. Close to the momenta with zero longitudinal and transverse momenta there is a large cloud of signals. This is where the long and short trajectories merge. By including a prefactor based on Born approximation the entire signals along the ring converge at the center of this cloud. On the other hand, the prefactor derived from Coulomb-Born approximation, which correctly accounts for the Coulomb effects, drives the signal cloud to the center of the ring. In momentum space this is the center of the classically allowed region. For some cases the signal at the circumference of the ring becomes weak, while for some other excitation states they are strongly preserved.

For both helium and argon, there are about 1.25 a.u. shifts between the positions of the peaks in the Born and Coulomb-Born approximation. This shift could be explained intuitively by comparing the maxima of the electron-impact excitation cross section for these approximations at the effective potential, ionization potential energy, plus the electron momentum traverse energy. The positions of the peaks are related to the threshold energies of the excitations, but shifted differently in CB because of the different relation of the Coulomb enhancement to the structural factors for different atoms and for different states. The shift is about 0.5 a.u. between the transition amplitude for Coulomb-Born approximation and the simple man model. The recollision-excitation process is the first step in the RESI mechanism of NSDI, and our results should be taken into account when calculating RESI within SFA. We underline that the Born approximation is not appropriate for the first step of RESI, which can be improved using Coulomb-Born approximation for treating the electron-impact excitation of the atomic ion during recollision.

[1] Th. Weber *et al.*, Nature (London) **405**, 658 (2000).
[2] G. Sansone *et al.*, Nature (London) **465**, 763 (2010).
[3] S. R. Leone *et al.*, Nat. Photon. **8**, 162 (2014).
[4] I. Tikhomirov, T. Sato, and K. L. Ishikawa, Phys. Rev. Lett. **118**, 203202 (2017).
[5] J. Itatani *et al.*, Nature (London) **432**, 867 (2004).
[6] P. B. Corkum and F. Krausz, Nat. Phys. **3**, 381 (2007).
[7] M. Lein, J. Phys. B **40**, R135 (2007).
[8] M. Meckel *et al.*, Science **320**, 1478 (2008).
[9] A. D. Shiner *et al.*, Nat. Phys. **7**, 464 (2011).

[10] J. Xu, C. I. Blaga, K. Zhang, Yu H. Lai, C. D. Lin, T. A. Miller, P. Agostini, and L. F. DiMauro, Nat. Commun. **5**, 4635 (2014).
[11] M. G. Pullen *et al.*, Nat. Commun. **6**, 7262 (2015).
[12] P. B. Corkum, Phys. Rev. Lett. **71**, 1994 (1993).
[13] K. C. Kulander, J. Cooper, and K. J. Schafer, Phys. Rev. A **51**, 561 (1995).
[14] J. L. Krause, K. J. Schafer, and K. C. Kulander, Phys. Rev. Lett. **68**, 3535 (1992).
[15] C. Figueira de Morisson Faria and X. Liu, J. Mod. Opt. **58**, 1076 (2011).
[16] W. Becker, X. Liu, P. J. Ho, and J. H. Eberly, Rev. Mod. Phys. **84**, 1011 (2012).
[17] A. L'Huillier, L. A. Lompre, G. Mainfray, and C. Manus, Phys. Rev. Lett. **48**, 1814 (1982).
[18] A. l'Huillier, L. A. Lompre, G. Mainfray, and C. Manus, Phys. Rev. A **27**, 2503 (1983).
[19] B. Walker, B. Sheehy, L. F. DiMauro, P. Agostini, K. J. Schafer, and K. C. Kulander, Phys. Rev. Lett. **73**, 1227 (1994).
[20] R. Moshammer, B. Feuerstein, W. Schmitt, A. Dorn, C. D. Schroter, J. Ullrich, H. Rottke, C. Trump, M. Wittmann, G. Korn, K. Hoffmann, and W. Sandner, Phys. Rev. Lett. **84**, 447 (2000).
[21] A. Staudte, C. Ruiz, M. Schöffler, S. Schossler, D. Zeidler, Th. Weber, M. Meckel, D. M. Villeneuve, P. B. Corkum, A. Becker, and R. Dörner, Phys. Rev. Lett. **99**, 263002 (2007).
[22] D. N. Fittinghoff, P. R. Bolton, B. Chang, and K. C. Kulander, Phys. Rev. Lett. **69**, 2642 (1992).
[23] D. N. Fittinghoff, P. R. Bolton, B. Chang, and K. C. Kulander, Phys. Rev. A **49**, 2174 (1994).
[24] A. Talebpour, C.-Y. Chien, Y. Liang, S. Larochelle, and S. L. Chin, J. Phys. B **30**, 1721 (1997).
[25] T. Weber, M. Weckenbrock, A. Staudte, L. Spielberger, O. Jagutzki, V. Mergel, F. Afaneh, G. Urbasch, M. Vollmer, H. Giessen, and R. Dorner, Phys. Rev. Lett. **84**, 443 (2000).
[26] B. Feuerstein, R. Moshammer, D. Fischer, A. Dorn, C. D. Schröter, J. Deipenwisch, J. R. Crespo Lopez-Urrutia, C. Höhr, P. Neumayer, J. Ullrich, H. Rottke, C. Trump, M. Wittmann, G. Korn, and W. Sandner, Phys. Rev. Lett. **87**, 043003 (2001).
[27] V. L. B. de Jesus, B. Feuerstein, K. Zrost, D. Fischer, A. Rudenko, F. Afaneh, C. D. Schröter, R. Moshammer, and J. Ullrich, J. Phys. B **37**, L161 (2004).
[28] B. Bergues *et al.*, Nat. Commun. **3**, 813 (2012).
[29] A. Rudenko, V. L. B. de Jesus, Th. Ergler, K. Zrost, B. Feuerstein, C. D. Schroter, R. Moshammer, and J. Ullrich, Phys. Rev. Lett. **99**, 263003 (2007).
[30] A. Talebpour, S. Larochelle, and S. L. Chin, J. Phys. B **30**, L245 (1997).
[31] C. Cornaggia and Ph. Hering, Phys. Rev. A **62**, 023403 (2000).
[32] C. Figueira de Morisson Faria and M. Lewenstein, J. Phys. B **38**, 3251 (2005).
[33] A. Becker and F. H. M. Faisal, Phys. Rev. Lett. **89**, 193003 (2002).
[34] S. P. Goreslavskii, S. V. Popruzhenko, R. Kopold, and W. Becker, Phys. Rev. A **64**, 053402 (2001).
[35] D. I. Bondar, W. K. Liu, and M. Y. Ivanov, Phys. Rev. A **79**, 023417 (2009).
[36] Z. Chen, A.-T. Le, T. Morishita, and C. D. Lin, Phys. Rev. A **79**, 033409 (2009).
[37] Z. Chen, Y. Liang, and C. D. Lin, Phys. Rev. Lett. **104**, 253201 (2010).
[38] A. S. Maxwell and C. Figueira de Morisson Faria, Phys. Rev. Lett. **116**, 143001 (2016).
[39] I. C. Percival and M. J. Seaton, Proc. Cambridge Philos. Soc. **53**, 654 (1957).
[40] S. L. Haan, L. Breen, A. Karim, and J. H. Eberly, Phys. Rev. Lett. **97**, 103008 (2006).
[41] D. F. Ye, X. Liu, and J. Liu, Phys. Rev. Lett. **101**, 233003 (2008).
[42] A. Emmanouilidou, Phys. Rev. A **78**, 023411 (2008).
[43] T. Morishita, A.-T. Le, Z. Chen, and C. D. Lin, Phys. Rev. Lett. **100**, 013903 (2008).
[44] S. Micheau, Z. Chen, A.-T. Le, and C. D. Lin, Phys. Rev. A **79**, 013417 (2009).
[45] Y. Liu, D. Ye, J. Liu, A. Rudenko, S. Tschuch, M. Dürr, M. Siegel, U. Morgner, Q. Gong, R. Moshammer, and J. Ullrich, Phys. Rev. Lett. **104**, 173002 (2010).
[46] Y. Liu, S. Tschuch, A. Rudenko, M. Dürr, M. Siegel, U. Morgner, R. Moshammer, and J. Ulrich, Phys. Rev. Lett. **101**, 053001 (2008).
[47] E. Eremina *et al.*, J. Phys. B **36**, 3269 (2003).
[48] A. Emmanouilidou and A. Staudte, Phys. Rev. A **80**, 053415 (2009).
[49] D. F. Ye and J. Liu, Phys. Rev. A **81**, 043402 (2010).
[50] L. Zhang, X. Xie, S. Roither, D. Kartashov, Y. Wang, C. Wang, M. Schöffler, D. Shafir, P. B. Corkum, A. Baltuka, I. Ivanov, A. Kheifets, X. Liu, A. Staudte, and M. Kitzler, Phys. Rev. A **90**, 061401(R) (2014).
[51] T. Shaaran, M. T. Nygren, and C. Figueira de Morisson Faria, Phys. Rev. A **81**, 063413 (2010).
[52] T. Shaaran and C. Figueira de Morisson Faria, J. Mod. Opt. **57**, 11 (2010).
[53] T. Shaaran, B. B. Augstein, and C. Figueira de Morisson Faria, Phys. Rev. A **84**, 013429 (2011).
[54] T. Shaaran and C. Figueira de Morisson Faria, Phys. Rev. A **85**, 023423 (2012).
[55] C. Figueira de Morisson Faria, T. Shaaran, and M. T. Nygren, Phys. Rev. A **86**, 053405 (2012).
[56] A. M. Perelomov, V. S. Popov, and M. V. Terent'ev, Zh. Eksp. Teor. Fiz. **51**, 309 (1966) [Sov. Phys. JETP **24**, 207 (1967)].
[57] M. V. Ammosov, N. B. Delone, and V. P. Krainov, Zh. Eksp. Teor. Fiz. **91**, 2008 (1986) [Sov. Phys. JETP **64**, 1191 (1986)].
[58] C. Figueira de Morisson Faria, X. Liu, and W. Becker, Springer Ser. Chem. Phys. **85**, 65 (2007).
[59] A. Becker and F. H. M. Faisal, J. Phys. B **29**, L197 (1996).
[60] A. Burgess, D. G. Hummer, and J. A. Tully, Philos. Trans. R. Soc. London A **266**, 225 (1970).
[61] V. Regemorter, R. Astron. Soc. **121**, 213 (1960).